J Neurophysiol 118: 532–543, 2017.
First published March 29, 2017; doi:10.1152/jn.00106.2017.

RESEARCH ARTICLE | *Cellular and Molecular Properties of Neurons*

Contributions of space-clamp errors to apparent time-dependent loss of Mg^{2+} block induced by NMDA

Min-Yu Sun,[1] Mariangela Chisari,[6] Lawrence N. Eisenman,[2] Charles F. Zorumski,[1,3,4,5] and Steven J. Mennerick[1,3,4]

[1]*Department of Psychiatry, Washington University School of Medicine, St. Louis, Missouri;* [2]*Department of Neurology, Washington University School of Medicine, St. Louis, Missouri;* [3]*Department of Neuroscience, Washington University School of Medicine, St. Louis, Missouri;* [4]*Taylor Family Institute for Innovative Psychiatric Research, Washington University School of Medicine, St. Louis, Missouri;* [5]*Center for Brain Research in Mood Disorders, Washington University School of Medicine, St. Louis, Missouri; and* [6]*Department of Biomedical and Biotechnological Sciences, Section of Pharmacology, University of Catania, Catania, Italy*

Submitted 15 February 2017; accepted in final form 27 March 2017

Sun MY, Chisari M, Eisenman LN, Zorumski CF, Mennerick SJ. Contributions of space-clamp errors to apparent time-dependent loss of Mg^{2+} block induced by NMDA. *J Neurophysiol* 118: 532–543, 2017. First published March 29, 2017; doi:10.1152/jn.00106.2017.—*N*-methyl-D-aspartate receptors (NMDARs) govern synaptic plasticity, development, and neuronal response to insult. Prolonged activation of NMDARs such as during an insult may activate secondary currents or modulate Mg^{2+} sensitivity, but the conditions under which these occur are not fully defined. We reexamined the effect of prolonged NMDAR activation in juvenile mouse hippocampal slices. NMDA (10 μM) elicited current with the expected negative-slope conductance in the presence of 1.2 mM Mg^{2+}. However, several minutes of continued NMDA exposure elicited additional inward current at −70 mV. A higher concentration of NMDA (100 μM) elicited the current more rapidly. The additional current was not dependent on Ca^{2+}, network activity, or metabotropic NMDAR function and did not persist on agonist removal. Voltage ramps revealed no alteration of either reversal potential or NMDA-elicited conductance between −30 mV and +50 mV. The result was a more linear NMDA current-voltage relationship. The current linearization was also induced in interneurons and in mature dentate granule neurons but not immature dentate granule cells, dissociated cultured hippocampal neurons, or nucleated patches excised from CA1 pyramidal neurons. Comparative simulations of NMDA application to a CA1 pyramidal neuron and to a cultured neuron revealed that linearization can be explained by space-clamp errors arising from gradual recruitment of distal dendritic NMDARs. We conclude that persistent secondary currents do not strongly contribute to NMDAR responses in juvenile mouse hippocampus and careful discernment is needed to exclude contributions of clamp artifacts to apparent secondary currents.

NEW & NOTEWORTHY We report that upon sustained activation of NMDARs in juvenile mouse hippocampal neurons there is apparent loss of Mg^{2+} block at negative membrane potentials. However, the phenomenon is explained by loss of dendritic voltage clamp, leading to a linear current-voltage relationship. Our results give a specific example of how spatial voltage errors in voltage-clamp recordings can readily be misinterpreted as biological modulation.

Address for reprint requests and other correspondence: S. J. Mennerick, Washington Univ. School of Medicine, Dept. of Psychiatry, 660 S. Euclid Ave., Box 8134, St. Louis, MO 63110 (e-mail: menneris@wustl.edu).

space clamp; NMDA; hippocampal slices; NEURON simulation; CA1; dentate gyrus

N-METHYL-D-ASPARTATE RECEPTORS (NMDARs) remain an important topic of study because of their interesting biophysical and physiological properties, including incompletely described downstream effectors. The channel pore is blocked by physiological concentrations of Mg^{2+} ions at membrane potentials (V_m) near rest. The block is relieved by depolarization, leading to a characteristic current-voltage (*I-V*) relationship, including a region of negative-slope conductance at potentials negative to approximately −30 mV (Hestrin et al. 1990; Mayer et al. 1984; Nowak et al. 1984; Perouansky and Yaari 1993). When Mg^{2+} block is relieved, typically by activation of other ionotropic glutamate receptors, Ca^{2+} influx can trigger various biochemical cascades. The receptors play multiple roles in development and refinement of nervous system architecture, in plasticity of the mature nervous system (Cohen and Greenberg 2008; Hunt and Castillo 2012), and in damage resulting from overstimulation (Ghasemi and Schachter 2011; Hardingham and Bading 2010; Paoletti et al. 2013). Damage may involve not only excessive ion influx through NMDARs themselves—here referred to as the primary current—but also recruitment of secondary currents mediated by a separate channel(s) (Chen et al. 1997; Olah et al. 2009; Thompson et al. 2008; Weilinger et al. 2012, 2016).

Recruitment of secondary currents following sustained NMDAR activation has been proposed to occur either through ionotropic Ca^{2+} influx (Chen et al. 1997; Mrejeru et al. 2011; Olah et al. 2009) or through metabotropic functions not requiring NMDAR-mediated ion flow (Nabavi et al. 2013; Weilinger et al. 2016). Secondary currents themselves may be mediated by TRP family members, pannexin channels, potassium channels, or others (Mrejeru et al. 2011; Olah et al. 2009; Shah and Haylett 2002; Thompson et al. 2008; Weilinger et al. 2012, 2016; Zorumski et al. 1989).

Furthermore, sustained activation of some ligand-activated channels, including NMDARs, may lead to changes in the pore

properties (e.g., pore dilation; Banke et al. 2010; Chung et al. 2008; Ferreira and Faria 2016; Meyers et al. 2003). In the NMDAR channel pore, Mg^{2+} sensitivity may be reduced by second messengers or by mechanical stresses (Chen and Huang 1992; Singh et al. 2012; Wu and Johnson 2009; Zhang et al. 1996). Mechanical stress may in turn be produced by overt trauma or by prolonged channel activation and accompanying cell swelling. Because altered Mg^{2+} sensitivity may develop gradually, it could masquerade as an independent conductance activated by NMDA. Reduced Mg^{2+} block would dampen an important check on NMDAR activation at negative V_m.

Here we identify a technical confound easily mistaken for a secondary current or loss of Mg^{2+} block. At face value, the time-dependent and NMDA concentration-dependent current possesses features expected from a time-dependent loss of Mg^{2+} sensitivity of NMDARs. We first characterize the additional current and then show that simulations of distal dendrite activation can readily account for key properties. Although poor space clamp of dendrites has been observed in simulations and in direct recordings of dendrites previously (Poleg-Polsky and Diamond 2011; Spruston et al. 1993; Williams and Mitchell 2008), our results reveal a specific example of how working with morphologically complex neurons can lead to mistaken ideas about new biological phenomena.

MATERIALS AND METHODS

Slice preparation. Hippocampal slices were prepared from male postnatal day (P)20–P36 wild-type C57BL/6J mice (Jackson Laboratories). In accordance with protocols approved by the Washington University Animal Studies Committee, mice were anesthetized with isoflurane and decapitated. The brain was removed and glued onto a Leica VT1200 specimen holder. Sagittal (300 μm) slices were cut in ice-cold modified artificial cerebrospinal fluid (ACSF) (in mM: 87 NaCl, 75 sucrose, 25 glucose, 25 $NaHCO_3$, 2.5 KCl, 1.25 NaH_2PO_4, equilibrated with 95% O_2-5% CO_2 plus 0.5 $CaCl_2$, 3 $MgCl_2$; 320 mosM). Slices were then incubated at 32–34°C for 30 min in choline-based ACSF (in mM: 92 choline chloride, 25 glucose, 30 $NaHCO_3$, 2.5 KCl, 1.2 NaH_2PO_4, 20 HEPES, 2 thiourea, 5 Na ascorbate, 3 Na pyruvate, 2 $CaCl_2$, and 1 $MgCl_2$, equilibrated with 95% O_2-5% CO_2; 300 mosM) and subsequently stored at room temperature in regular ACSF (in mM: 125 NaCl, 25 glucose, 25 $NaHCO_3$, 2.5 KCl, 1.25 NaH_2PO_4, equilibrated with 95% O_2-5% CO_2 plus 2.6 $CaCl_2$, 1.2 $MgCl_2$; 310 mosM), allowing for at least 1-h recovery before experiments. Except for noted exceptions, drugs were obtained from Sigma (St. Louis, MO).

Whole cell patch-clamp recording in slices. Slices were transferred to a recording chamber and continuously perfused with oxygenated regular ACSF at 2 ml/min. Experiments were performed at 30–32°C. In all experiments, 2,3-dioxo-6-nitro-1,2,3,4-tetrahydrobenzo[*f*]quinoxaline-7-sulfonamide (NBQX, 10 μM; Tocris, Bristol, UK), picrotoxin (100 μM; Tocris), and D-serine (10 μM) were included in extracellular solutions to inhibit AMPA receptor- and GABA receptor-mediated neurotransmission and to enhance NMDAR-mediated currents. For the experiments in Fig. 2*C*, D-serine (10 μM) was initially included in extracellular solutions and later removed at the indicated time point. (+)-5-Methyl-10,11-dihydro-5*H*-dibenzo[*a*,*d*]cyclohepten-5,10-imine (MK-801, 40 μM; Tocris) or 1 μM CGP-78608 (Tocris) was bath-applied to examine effects of NMDAR channel block. For experiments assessing effects of zero extracellular Ca^{2+}, regular ACSF with 0 mM $CaCl_2$ and 0.5 mM BAPTA (Life Technologies, Carlsbad, CA) was bath-applied for at least 10 min before data collection was initiated. For experiments assessing tetrodotoxin (TTX) effects, 1 μM TTX (Tocris) was bath-applied for at least 10 min before recording.

Somatic whole cell patch-clamp recordings were performed with standard differential interference contrast microscopy under infrared illumination. CA1 pyramidal cells, interneurons, or dentate granule cells (DGCs) were identified on an upright Nikon Eclipse E600FN microscope and a QImaging camera controlled with QCapture (QImaging, Surrey, BC, Canada). Somatic whole cell recordings were made with borosilicate patch pipettes (World Precision Instruments, Sarasota, FL; Sutter Instruments, Novato, CA), having open tip resistance of 3–7 MΩ. After a whole cell configuration was established, cells were allowed to fill with the intracellular solution for ~5 min. Recordings were obtained with a MultiClamp 700B amplifier (Molecular Devices; Sunnyvale, CA) and pCLAMP 10.4 software (Molecular Devices).

The intracellular pipette solution contained (in mM) 120 cesium methanesulfonate, 20 HEPES, 10 EGTA, 2 MgATP, 0.3 Na_2GTP, and 5 QX-314 (pH adjusted with CsOH to pH 7.25; 290 mosM). QX-314 was omitted for measuring sodium current in a subset of dentate granule neurons. For NMDAR current, cells were voltage-clamped at −30 mV, and data were acquired in gap-free mode. Pipette capacitance was adjusted with MultiClamp 700B Commander software. Access resistance was not compensated. For assessing *I-V* relationships, from a command voltage (V_{com}) of −30 mV cells were hyperpolarized to −70 mV for 10–100 ms, and a +120-mV ramp (120 mV/s) was then applied. For measuring Na^+ current in DGCs, peak current in response to a voltage pulse (50 ms) from −90 mV to −10 mV was quantified.

Data were acquired at 2 kHz, filtered at 1 kHz with an eight-pole Bessel filter, and digitized with a DigiData1550 16-bit A/D converter (Molecular Devices). Somatic access resistance was monitored continuously, and cells with unstable access resistance (>20% change) were excluded from analysis.

Cell culture. All animal care and experimental procedures were consistent with National Institutes of Health guidelines and were approved by the Washington University Animal Studies Committee. Studies involving animals are reported in accordance with the ARRIVE guidelines for reporting experiments involving animals (Kilkenny et al. 2010; McGrath et al. 2010). Rat hippocampal cultures were prepared from P1–P3 pups of both sexes (85% female) anesthetized with isoflurane. Hippocampal slices (500-μm thickness) were digested with 1 mg/ml papain in oxygenated Leibovitz L-15 medium (Life Technologies, Gaithersburg, MD). Tissue was mechanically triturated in modified Eagle's medium (MEM; Life Technologies) containing 5% horse serum, 5% FCS, 17 mM D-glucose, 400 μM glutamine, 50 U/ml penicillin, and 50 μg/ml streptomycin. Astrocytes and neurons were seeded in MEM at a density of ~600 cells/mm^2 onto 25-mm cover glasses coated with 0.1 mg/ml poly-D-lysine and 1 mg/ml laminin. Cultures were incubated at 37°C in a humidified chamber with 5% CO_2-95% air. Cytosine arabinoside (6.7 μM) was added 3–4 days after plating to inhibit glial proliferation. The following day, half of the culture medium was replaced with Neurobasal medium (Life Technologies) plus B27 supplement (Life Technologies).

Whole cell patch-clamp recording in neuron cultures. Whole cell recordings were made with an Axopatch 200B amplifier (Molecular Devices) at room temperature at days in vitro 6–13 (Mennerick et al. 1995). Cells were recorded in regular ACSF containing (in mM) 138 NaCl, 10 glucose, 4 KCl, 2 $CaCl_2$, 1 $MgCl_2$, 10 HEPES, 0.001 NBQX, 0.1 picrotoxin, and 0.01 D-serine, pH 7.25. Whole cell pipette solutions contained (in mM) 120 cesium methanesulfonate, 20 HEPES, 10 EGTA, 2 MgATP, 0.3 Na_2GTP, and 5 QX-314 (pH adjusted with CsOH to pH 7.25; 290 mosM). NBQX (10 μM), picrotoxin (100 μM), and D-serine (10 μM) were included in extracellular solutions as described above. For application of NMDA (100 μM) to whole cells, a multibarrel solution exchange system with a common delivery tip was used (Warner Instruments). The common tip was placed 0.5 mm from the center of the microscope field. Experiments were performed at room temperature, and quantification of whole cell current response

to a voltage ramp (−70 mV to +50 mV, 1 s) was used to quantify data.

Nucleated outside-out patches. To isolate nucleated patches, after a somatic whole cell recording from CA1 neurons in slices was established, negative pressure (70–200 mbar) was applied and the patch pipette was withdrawn slowly. A small negative pressure (10–30 mbar) was maintained during the recording. The resulting nucleated patch was verified visually as a sphere at the pipette tip. Nucleated patches were held at −30 mV throughout the experiment except for voltage ramps in the absence and presence of NMDA as described above.

NEURON simulations. We performed simulations by adapting and modifying a CA1 pyramidal cell model published previously (Poirazi et al. 2003a, 2003b) and available from the NEURON database (https://senselab.med.yale.edu/ModelDB/ShowModel.cshtml?model=20212). We used the default pyramidal cell morphology, which included detailed dendritic structure but without spines and the existing ion channel set. However, we set the conductance of HH channels and all the potassium channels to be zero, to mimic channel blockers used in the cesium-based pipette solution with QX-314. Remaining conductances included four types of voltage-gated Ca^{2+} channels and passive conductance with kinetic properties and distributions across the cell as previously documented (Poirazi et al. 2003a, 2003b). We simulated a single-electrode voltage clamp at the soma with a 10-MΩ access resistance.

The simulated NMDA conductance was taken from a simplified two-state model that produced realistic Mg^{2+} sensitivity but no desensitization (Destexhe et al. 1998):

$$C + T \underset{\beta}{\overset{\alpha}{\rightleftharpoons}} O$$

T is an agonist (transmitter) that interacts with the unbound form of the receptor C, leading to the open state O. α and β are voltage-independent forward and backward rate constants (10 $mM^{-1}ms^{-1}$ and 0.0125 ms^{-1}, respectively). γ is the fraction of open receptors and can be described by $d\gamma/dt = \alpha[T](1 - \gamma) - \beta\gamma$, where $[T]$ is the concentration of transmitter. The NMDA current is described by $I_{NMDA} = g_{max}B(V)\gamma(V - E_{NMDA})$, where g_{max} is the maximal conductance of NMDARs, $B(V)$ is the fraction of NMDAR conductance not blocked by Mg^{2+}, V is the postsynaptic voltage, and $E_{NMDA} = 0$ mV is the reversal potential. The Mg^{2+} block in turn was expressed as an instantaneous function of voltage, similar to previous descriptions (Jahr and Stevens 1990): $B(V) = 1/[1 + 0.33[Mg^{2+}]_o\exp(-0.06V)]$, where $[Mg^{2+}]_o$ is the external magnesium concentration in millimolar and V is the voltage in millivolts.

For purposes of our simulations, we used the default saturating concentration of agonist ($[T] = 1$ mM), which yields a fraction of open receptors of ~0.99. We then adjusted the g_{max} (maximum conductance) value in the various compartments to yield experimentally observed steady-state current values at −30 mV. To simulate the onset of NMDA-elicited current, a pulse command was inserted to initiate NMDA conductance. To obtain current at different voltages we pulsed V_m from an initial V_{com} of −30 mV to values from −70 mV to +50 mV for 3.5 s. Current in the absence of NMDA ($g_{max} = 0$) was subtracted to generate data shown in *I-V* plots.

Early, middle, and late time points of experimental NMDA perfusion were simulated by changing the maximum conductance density in various compartments to simulate differential accessibility of soma and dendrites to NMDA. To mimic early time points, NMDAR maximum conductance density at soma and proximal dendrites was initially set to 0.27 mS/cm^2 and was set to 0.145 mS/cm^2 in distal dendrites, representing the early phase of recordings. We reasoned that the soma and proximal dendrites of recorded cells are near the surface and have most immediate access to the full NMDA concentration. Dendrites other than the distal tufts have a density of NMDARs similar to the soma (Andrasfalvy and Magee 2001; Otmakhova et al. 2002). Thus we increased conductance density at distal dendrites to 0.27 mS/cm^2 to simulate middle time points where the full concentration had reached most dendrites. To simulate the latest time points, we increased the conductance density to 0.55 mS/cm^2 at the deep distal tufts, which have been shown to have approximately double the NMDAR density of other somatodendritic regions (Bittner et al. 2012; Otmakhova et al. 2002).

In separate simulations, we modeled cultured neurons by removing dendritic branches from the main apical dendrite. We evaluated the sufficiency of the reduced CA1 model to represent a cultured neuron by comparing the passive capacitive responses to a hyperpolarizing voltage pulse as described in RESULTS and in previous work (Mennerick et al. 1995).

Data analysis. Data analysis was performed in Clampfit 10.4 (Molecular Devices). For calculating the I_{-70mV}-to-I_{-30mV} ratio, we used current before any voltage change to quantify I_{-30mV} and current during the −70 mV dwell time (before the onset of the voltage ramp) as I_{-70mV}. NMDA current was isolated by digital subtraction. Baseline current used for subtraction was obtained from the same voltage protocols performed either before NMDA or after NMDA as shown in Figs. 1–3 and also described in RESULTS. *I-V* curves were derived from the unsubtracted or subtracted current output of the ramp protocol as described in RESULTS and figures.

Student's independent two-tailed *t*-test was performed to determine statistical significance between the means of two groups. For multiple-group (>2 groups) comparison, one-way ANOVA and Bonferroni post hoc analyses were performed. For detection of effects within cells, a paired *t*-test was performed. For comparison of induced and residual currents at −70 mV within and between conditions of NMDAR blockade, a mixed-design ANOVA and Bonferroni post hoc analysis were performed. Significance is described at the level of $P \leq 0.05$, 0.01, and 0.001. Values are presented as means ± SE.

RESULTS

Prolonged NMDA application at moderate concentration elicits additional current at negative membrane potentials. Excessive activation of NMDARs contributes to damage in stroke, traumatic brain injury, and other disorders. We examined the potential downstream consequences of excessive activation by applying NMDA (7.5–10 μM) to CA1 pyramidal neurons in juvenile mouse hippocampal slices in the presence of 1.2 mM Mg^{2+} and assessing the resultant current at −30 mV, a potential at which Mg^{2+} block is relieved. The presence of Mg^{2+} permitted direct observation of current in the recorded cell without overstimulating the entire network in the absence of Mg^{2+}, which can result in network hyperexcitability (Walther et al. 1986). Before and during NMDA application, a voltage ramp (120 mV, 1 s) was applied. The ramp helped to identify changes in current during the presentation of NMDA that might not be evident at a single V_m value. Voltage-gated sodium and potassium currents were blocked with QX-314 and Cs^+, respectively, in the pipette solution. The initial current rectified as expected, evidenced by smaller current at −70 mV than at −30 mV (Fig. 1, *A2* − *A1* and *B*). At a later time point inward current increased at −70 mV (Fig. 1, *A3* − *A1* and *B*) without commensurate change at −30 mV, although there was often a decrease in current noise at −30 mV (Fig. 1, *A2* vs. *A3*). The change in noise perhaps indicated altered NMDAR channel behavior (Anderson and Stevens 1973) or participation of additional channel type(s). No consistent change in access resistance was correlated with the decrease in noise. The increase of current ratio measured at −70 mV vs. −30 mV (I_{-70mV}/I_{-30mV}) was NMDA concentration dependent as well as time dependent, as application of NMDA at 100 μM

increased inward current within a much shorter time frame (Fig. 1*B*).

NMDA-induced current is significantly blocked after NMDAR blockade or washout of NMDA. We first considered the possibility that additional inward current at −70 mV is a secondary current, defined by persistence following NMDA removal (Chen et al. 1997; Thompson et al. 2008) and/or by activation by metabotropic function of NMDARs (Weilinger et al. 2016). To elucidate whether the increased inward current at −70 mV persists independent of continued NMDAR activation, we washed out NMDA after induction of additional current at −70 mV (Fig. 2, *A* and *B*). After removal of NMDA, current at −30 mV completely recovered to baseline (Fig. 2*A*) and inward current at −70 mV also significantly decreased (Fig. 2, *B* and *F*). To test whether persisting current at −70 mV can explain time-dependent changes in NMDA current, we subtracted ramp-induced current after removal of NMDA from early and late NMDA time points (*A1*, *A2* in Fig. 2*A*) in eight cells. We observed a change in current ratio similar to that in Fig. 1*B*, where subtraction of current before NMDA application was performed. We thus conclude that persisting secondary current cannot explain the time-dependent change in NMDA current at −70 mV. Furthermore, we observed no change in reversal potential of current from early to late time points (Fig. 2*B*).

As another test of secondary current participation, we tested reversibility of the current with different classes of antagonist (Fig. 2, *C* and *D*). After the increase of current at −70 mV (Fig. 2C, *C1* − *C2*; Fig. 2*D*, *D1* − *D2*), blocking either putative metabotropic NMDAR function with the glycine-binding site antagonist CGP-78608 (Weilinger et al. 2016) or ionotropic NMDAR function with the channel blocker MK-801 significantly reduced the current at −70 mV (Fig. 2, *C*, *D*, and *F*), suggesting that the majority of current at −70 mV arises directly from NMDARs. The blocking effect of MK-801 was indistinguishable from antagonism of CGP-78608, suggesting that the inward current at −70 mV is unlikely to be generated through metabotropic function of NMDARs, which requires agonist/coagonist binding but not channel function (Weilinger et al. 2016). To verify this conclusion, we pretreated slices with 40 μM MK-801 (>30 min to allow for use-dependent block) and then applied 100 μM NMDA. In the presence of MK-801, NMDA failed to induce any current at −30 mV (Fig. 2*E*; 2.3 ± 5.7 pA, $n = 5$ cells within 15–20 min of NMDA application) or additional current at −70 mV (2.6 ± 5.6 pA, $n = 5$ cells within 15–20 min of NMDA application), suggesting that ionotropic NMDAR function is required for the induction of the inward current at −70 mV. By contrast, in the absence of MK-801, current amplitude at −70 mV was 1,446.5 ± 249.2 pA ($n = 7$). These results differ from some previous observations in which MK-801 failed to block induction or maintenance of secondary current (Weilinger et al. 2016).

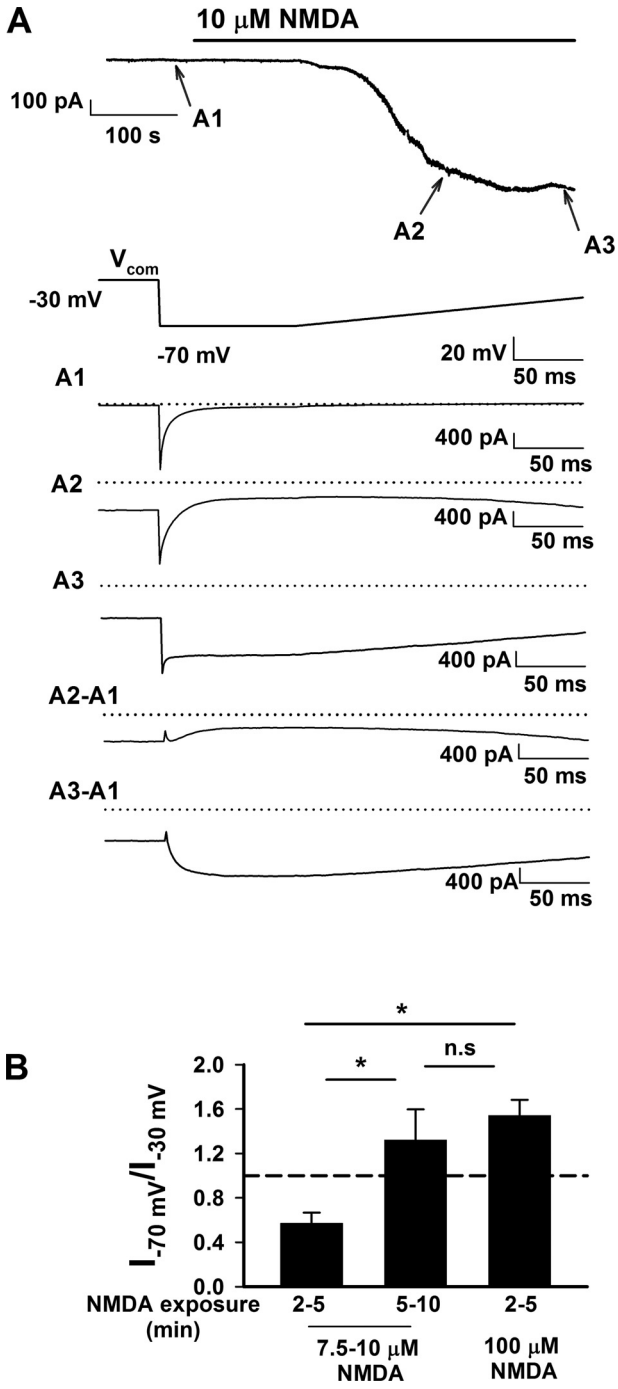

Fig. 1. NMDA (7.5–10 μM) elicits time-dependent current at negative V_m. *A*: changes to NMDA-elicited current at −30 and −70 mV. *Top*: application of 10 μM NMDA elicited a tonic current at −30 mV. The points indicated by labeled arrows indicate times at which voltage ramps were executed. The currents during ramps have been excised but are shown at higher resolution below. The next trace indicates the ramp voltage command (V_{com}). *A1* corresponds to time point indicated by arrow in *top* trace, before NMDA application. *A2*: total, unsubtracted current at *time point A2* in *top* trace. *A3*: total, unsubtracted current at a later time point in *top* trace. Two *bottom* traces are digital subtractions as indicated. The current preceding NMDA application was subtracted from current at the 2 time points during NMDA application. The NMDA-induced current at −30 mV changed relatively little, but the inward current at −70 mV grew substantially and changed polarity with respect to current at −30 mV. Dotted lines represent current value at 0. *B*: summary of time- and concentration-dependent changes in the relationship between NMDA-elicited current at −70 mV and that at −30 mV. The I_{-70mV}-to-I_{-30mV} ratio was <1 when measured within 5 min of NMDA application (7.5–10 μM), indicating negative-slope conductance. However, after longer exposure to NMDA (>5 min), I_{-70mV}/I_{-30mV} became >1, commensurate with addition of current at −70 mV. The inward current was detected in 100 μM NMDA more rapidly, with a shorter latency (<5 min) following the onset of NMDA application ($n = 10$ for 7.5–10 μM NMDA-treated cells; $n = 7$ for 100 μM NMDA-treated cells). *$P \leq 0.05$. n.s., Not significant.

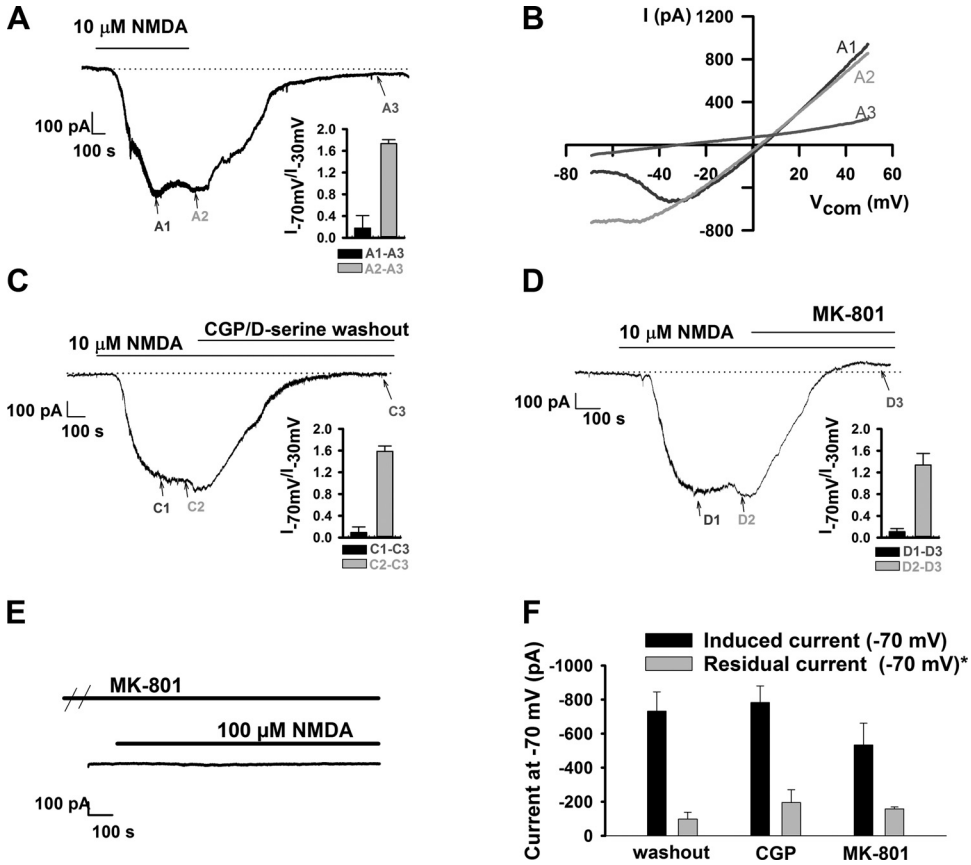

Fig. 2. NMDA-induced linear current is driven by NMDARs and does not represent persisting secondary current. *A*: current elicited by 10 μM NMDA at -30 mV. After growth of inward current at -70 mV (verified by I_{-70mV}/I_{-30mV}; see *inset*: *A1* $-$ *A3* vs. *A2* $-$ *A3*), NMDA was washed out, and the current was allowed to recover to baseline (*A3*). To ascertain whether the increase in current at -70 mV resulted from a persisting secondary current, the current following washout was subtracted from current at *time points A1* and *A2*, and the resulting I_{-70mV}/I_{-30mV} was calculated (*inset*; $n = 8$). The resulting current ratios suggest that the increase in current at -70 mV cannot be explained by persisting secondary current. *B*: unsubtracted voltage ramp responses are shown from the cell in *A*. *C*: same protocol as *A*, except that glycine/D-serine-site antagonist 1 μM CGP-78608 was applied and D-serine washed out. This treatment also reversed the current at -30 mV. The indicated current subtractions revealed a change in I_{-70mV}/I_{-30mV} that was not explained by persisting secondary current (*inset*; $n = 6$). *D*: tonic current elicited by 10 μM NMDA at -30 mV. After current linearization, 40 μM MK-801 was applied, completely abolishing the current at -30 mV. Again, subtraction revealed a time-dependent change in current ratios not explained by persisting current ($n = 5$). *E*: MK-801 pretreatment completely blocked current induction by 100 μM NMDA at both -30 mV (shown) and -70 mV (assayed by ramps, not shown; see RESULTS), excluding involvement of metabotropic NMDAR function. *F*: current induced at -70 mV during NMDA exposure vs. residual current after washout or antagonism in *A*, *C*, and *D*. Residual current was measured relative to pre-NMDA levels ($^*P < 0.05$). A persisting current was evident at -70 mV, but it was much smaller than that induced during NMDA application.

In all cases in which NMDA induced additional current at -70 mV (Fig. 2, *A–D*), we observed a small persistent inward current at -70 mV after NMDA washout/antagonism (Fig. 2*F*, residual current). However, the residual current was much smaller than the current induced at -70 mV in the presence of NMDA (Fig. 2*F*, induced current). This analysis suggests that although small secondary current was induced, maintenance of a current mediated by a persistently activated separate channel or by damage is a relatively minor contributor to the NMDA-induced current at -70 mV. Our results suggest that ionotropic function of NMDARs is required to induce and maintain additional current at -70 mV during NMDA application, either because NMDARs themselves underlie the current or because continuous NMDAR activation is required to sustain the current.

Time-dependent current linearization is independent of Ca^{2+} influx and network activity. Given that additional current appears to require ionotropic NMDAR function, we focused on a potential role for Ca^{2+} influx. Ca^{2+}-induced secondary current has been supported by some studies (Chen et al. 1997; Mrejeru et al. 2011; Olah et al. 2009; Zorumski et al. 1989) but not others (Thompson et al. 2008; Weilinger et al. 2012, 2016). To test a role for Ca^{2+} influx through NMDARs, we removed Ca^{2+} and applied 0.5 mM BAPTA in the extracellular solution. As shown in Fig. 3, development of additional current at negative V_m did not differ from recordings in normal extracellular Ca^{2+} concentration (Fig. 3, *A* and *B*). On the basis of these findings, we conclude that the development of linear current is mediated by ionotropic NMDAR function but is independent of Ca^{2+} influx.

Given the insensitivity to manipulation of Ca^{2+} influx, the late induced conductance appears to be directly activated by NMDAR activation rather than by secondary neurotransmitter release. To further test this conclusion, we applied 1 μM TTX to suppress network activity and examined the *I-V* relationship during 10 μM NMDA application. Suppression of network activity did not prevent current development or linearization of the *I-V* relationship (Fig. 3, *C* and *D*), supporting the idea that current development is directly mediated by NMDAR activation.

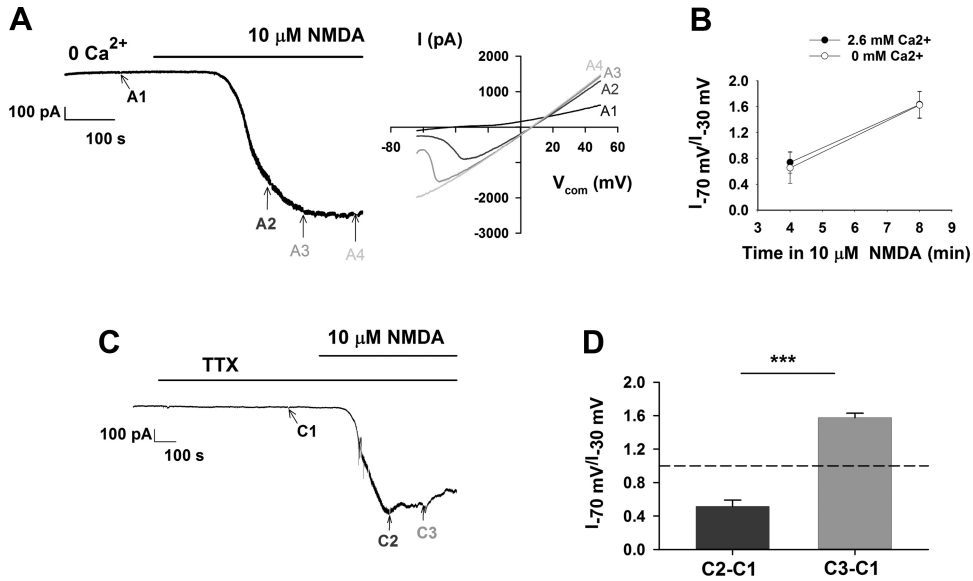

Fig. 3. NMDA-induced linear current is independent of Ca^{2+} influx or network activity. *A*: in the presence of nominally Ca^{2+}-free bath solution, 10 μM NMDA-induced tonic current still linearized (*A2–A4*). *Left*: representative trace of NMDA-induced tonic current at −30 mV. *Right*: *I-V* curve measured at points denoted by *A1–A4*. *B*: time-dependent linearity change of NMDAR current elicited at typical (2.6 mM) or reduced (0 mM) extracellular Ca^{2+} concentration ($[Ca^{2+}]_o$). I_{-70mV}/I_{-30mV} measured 4 min and 8 min after 10 μM NMDA application were compared between the 2 $[Ca^{2+}]_o$ values. No significant difference of I_{-70mV}/I_{-30mV} was observed at either time point between the 2 groups. ($n = 7$ for 2.6 mM Ca^{2+} group; $n = 4$ for 0 mM Ca^{2+} group). *C*: when 1 μM TTX was bath applied, 10 μM NMDA induced a tonic current at −30 mV, which linearized (*C2* to *C3*). *D*: comparison of I_{-70mV}/I_{-30mV} between *C2* and *C3* reflects a significant increase of current linearity. These results suggest that suppression of network activity by 1 μM TTX does not prevent current linearization ($n = 7$; $^{***}P < 0.001$).

NMDA-induced linear current is present only in morphologically complex neurons. To test the generality of the NMDAR-induced inward current at −70 mV, we challenged additional cell types with 100 μM NMDA: mature and immature dentate granule neurons, CA1 stratum radiatum interneurons, neurons in dissociated cell culture, and nucleated patches from CA1 neurons in slices. Mature and immature dentate granule neurons were identified on the basis of previous work (Liu et al. 1996, 2000). We divided granule cells from the inner blade of the dentate and the subgranular zones into those with input resistance < 1 GΩ (mature) and those with input resistance > 1 GΩ [immature; 0.33 ± 0.03 GΩ ($n = 13$) vs. 2.26 ± 0.28 GΩ ($n = 11$)]. Maturational state was further verified in a subset of cells by inward sodium current evoked by voltage pulses to −10 mV; mature dentate cells exhibited significantly larger inward sodium current than immature cells [3,743.9 ± 401.4 pA ($n = 6$) vs. 223.6 ± 144.0 pA ($n = 4$); Fig. 4, *A* and *B*, *insets*] (Mongiat et al. 2009). Cell capacitance was also significantly smaller in immature neurons [28.6 ± 4.9 pF ($n = 7$ mature neurons) vs. 4.9 ± 0.5 pF ($n = 6$ immature neurons)]. NMDA induced linear *I-V* curves in mature dentate granule neurons but not in immature cells (Fig. 4, *A*, *B*, *F*). Moreover, 100 μM NMDA induced significantly larger current in the mature DGCs than in the immature DGCs [487.4 ± 82.3 pA ($n = 13$ mature DGCs) vs. 33.5 ± 8.9 pA ($n = 11$ immature DGCs)]. We examined another class of mature neurons, CA1 stratum radiatum interneurons. These cells also exhibited linearization similar to CA1 pyramidal neurons and mature granule cells ($n = 3$ interneurons; Fig. 4, *C* and *F*).

Previously, prominent NMDAR-induced secondary currents have been demonstrated in cultured neurons (Chen et al. 1997; Thompson et al. 2008; Weilinger et al. 2016). We applied NMDA to dissociated hippocampal neurons cultured for 6–13 days. We found apparent time-dependent linearization in the NMDA-induced currents. However, unlike CA1 pyramidal cells in slices, NMDA-induced currents did not fully reverse upon washout (Fig. 4*D*; −131 ± 58 pA, $n = 5$). To account for this persistent current, we subtracted it from total current in the presence of NMDA. Subtracted, NMDAR-induced currents remained nonlinear, unlike cells from slices (Fig. 4, *D* and *F*). We conclude that, compared with neurons in juvenile mouse slices, cells in culture exhibit a stronger persisting bona fide secondary current that does not require ongoing NMDAR activity for maintenance. However, once the persisting current was accounted for, the *I-V* relationship of NMDA responses in cultured neurons remained nonlinear.

Our results suggest that morphologically complex, mature neurons exhibit linearization of NMDA-induced current while less complex or immature neurons maintain a canonical nonlinear *I-V* profile. To test whether the nonlinear to linear conversion is maintained in excised membrane from CA1 pyramidal neurons, we excised nucleated patches from these cells in slices (Sather et al. 1992). Somatic nucleated patches exhibited a more nonlinear *I-V* relationship than intact mature DGCs (Fig. 4, *E* and *F*; $P < 0.001$), although rectification tended to be slightly weaker than in immature DGCs and cultured neurons (Fig. 4*F*; $P > 0.05$).

We considered two potential explanations for the time-dependent development of NMDAR-induced currents at negative V_{com}. First, we considered the possibility that mature synaptic NMDARs on dendrites exhibit a concentration-dependent and time-dependent alteration of NMDAR pore properties, resulting in loss of Mg^{2+} block (Chen and Huang 1992; Wu and Johnson 2009; Zhang et al. 1996). This mechanism would explain the lack of change of NMDAR-elicited membrane conductance at V_{com} values of −30 mV through +50 mV (Fig. 2*B*, Fig. 3*A*). Second, we considered the possibility that strong activation of NMDARs may cause time-dependent

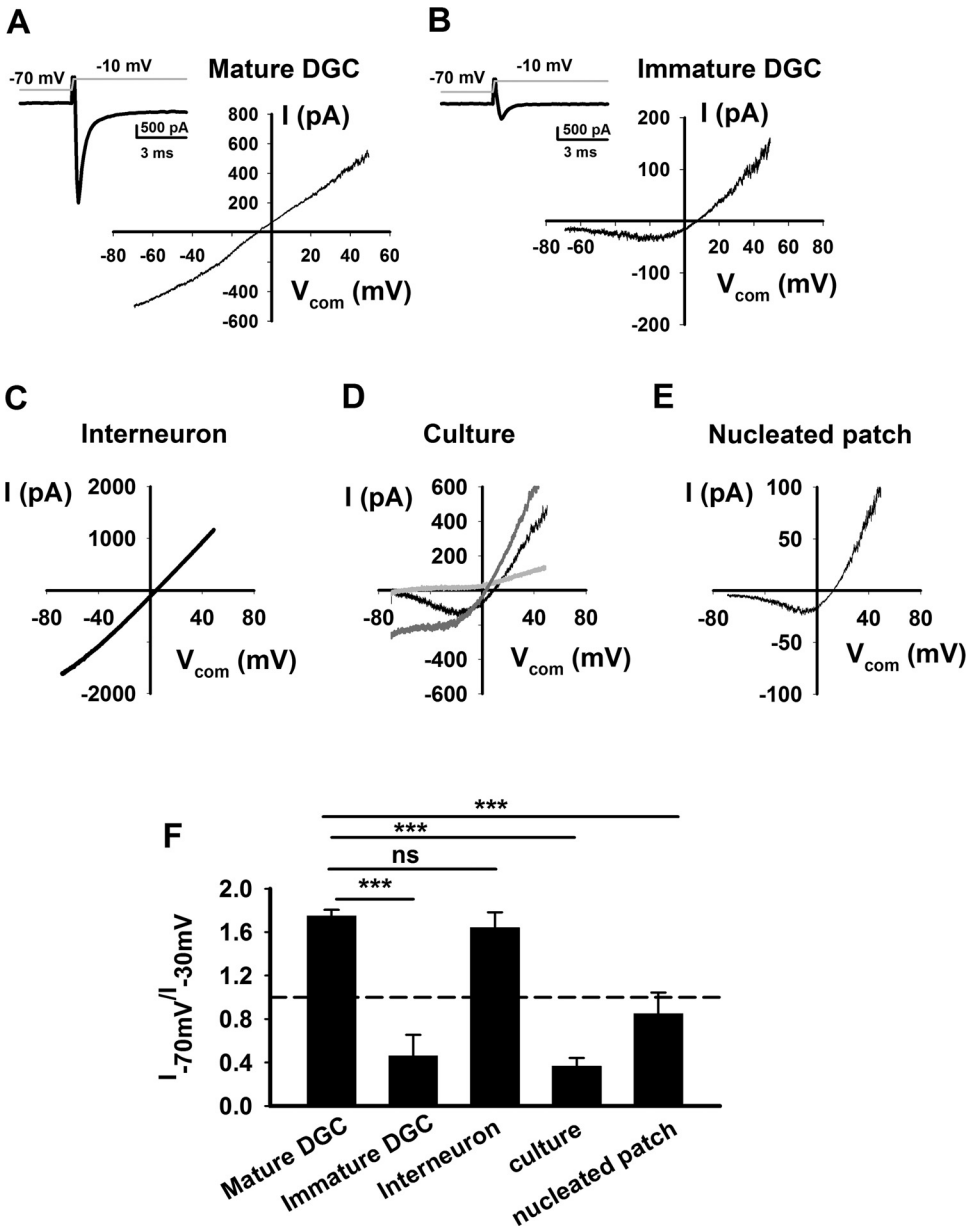

Fig. 4. NMDA-induced linear current was observed in morphologically complex neurons but not in neurons with simplified morphology. *A*: subtracted *I-V* curve elicited by a ramp voltage command during sustained current induced by 100 μM NMDA at −30 mV in a mature dentate granule cell (DGC). Current in the absence of NMDA (before application) was digitally subtracted. The cell exhibited an input resistance < 1 GΩ and robust voltage-gated sodium current with a voltage pulse to −10 mV (*inset*). Subtracted NMDAR currents elicited in the mature DGCs exhibited linear *I-V* relationships. *B*: same protocol from an immature DGC with an input resistance >1 GΩ and weak excitability evidenced by small sodium current (*inset*). *C*: subtracted *I-V* obtained during application of 100 μM NMDA at −30 mV in a CA1 stratum radiatum interneuron. *D*: *I-V* curve from a tonic current elicited by 100 μM NMDA at −30 mV in a cultured hippocampal neuron taken from a postnatal day 1 rat and cultured for 13 days. Light gray trace represents current in the absence of NMDA before NMDA application. Dark gray trace represents residual current after washout after 5-min NMDA application. Because of the substantial secondary current evident in cultured neurons, black trace represents total current during NMDA application minus the residual current after washout to isolate the NMDA-induced *I-V* relationship unrelated to persisting secondary current. *E*: subtracted *I-V* curve elicited during application of 100 μM NMDA in a nucleated patch excised from a CA1 neuron. *F*: quantification and comparison of current linearity in the range of −30 mV to −70 mV, measured as $I_{-70\text{mV}}/I_{-30\text{mV}}$—between mature ($n = 13$) and immature ($n = 11$) DGCs, interneurons ($n = 3$), cultured hippocampal neurons ($n = 6$), and nucleated patches from CA1 neurons in slices ($n = 11$; $^{***}P < 0.001$). The difference between nucleated patches and immature granule neurons or cultured cells was not statistically significant ($P > 0.05$).

loss of voltage clamp, which results in the linearization profile observed. Although the second possibility is perhaps more likely, several aspects of a space-clamp explanation were difficult to explain intuitively. First, current was altered mainly in the range of V_{com} values more negative than −30 mV; conductance in the range of −30 mV to +50 mV was mostly unaffected (Fig. 2, Fig. 3). Second, why a space-clamp error should exhibit time dependence at the NMDA concentrations employed was not immediately evident. Third, the change in membrane noise at −30 mV typically accompanying induction of linearized current suggested a change in channel behavior. Finally, it was not apparent why escape from clamp would not result in a detectable shift in the overall I_{NMDA} reversal potential.

NMDA linearization is recapitulated by spatial voltage errors simulated in a CA1 model cell. To test whether a space-clamp explanation can account for these observations, we used a previously published model of a CA1 pyramidal neuron (Fig. 5*A*, Fig. 6*A*; Poirazi et al. 2003a, 2003b). First, we simulated tonic activation of NMDARs throughout the entire model cell, with a progressive increase in NMDA conductance from proximal to distal dendritic compartments to mimic experimentally relevant current amplitudes (Fig. 5). The NMDAR conductance mechanism was previously used by others (Destexhe et al. 1998; Poirazi et al. 2003a, 2003b). To mimic the block of voltage-gated sodium and potassium currents in our experiments, we removed the Hodgkin-Huxley sodium and potassium conductances, as well as I_{h}, I_{kca}, I_{mAHP}, I_{km}, I_{ap}, and I_{ad}, as defined previously (Poirazi et al. 2003a, 2003b). Remaining voltage-gated conductances included several classes of Ca^{2+} channels (Poirazi et al. 2003a, 2003b).

Introduction of NMDA conductance into only the somatic compartments (12.56 mS/cm^2) produced a typical NMDAR *I-V* relationship, with a region of clear negative-slope conductance (Fig. 5, *A–C*). However, increasing the NMDA conductance in dendrites to simulate time-dependent recruitment of

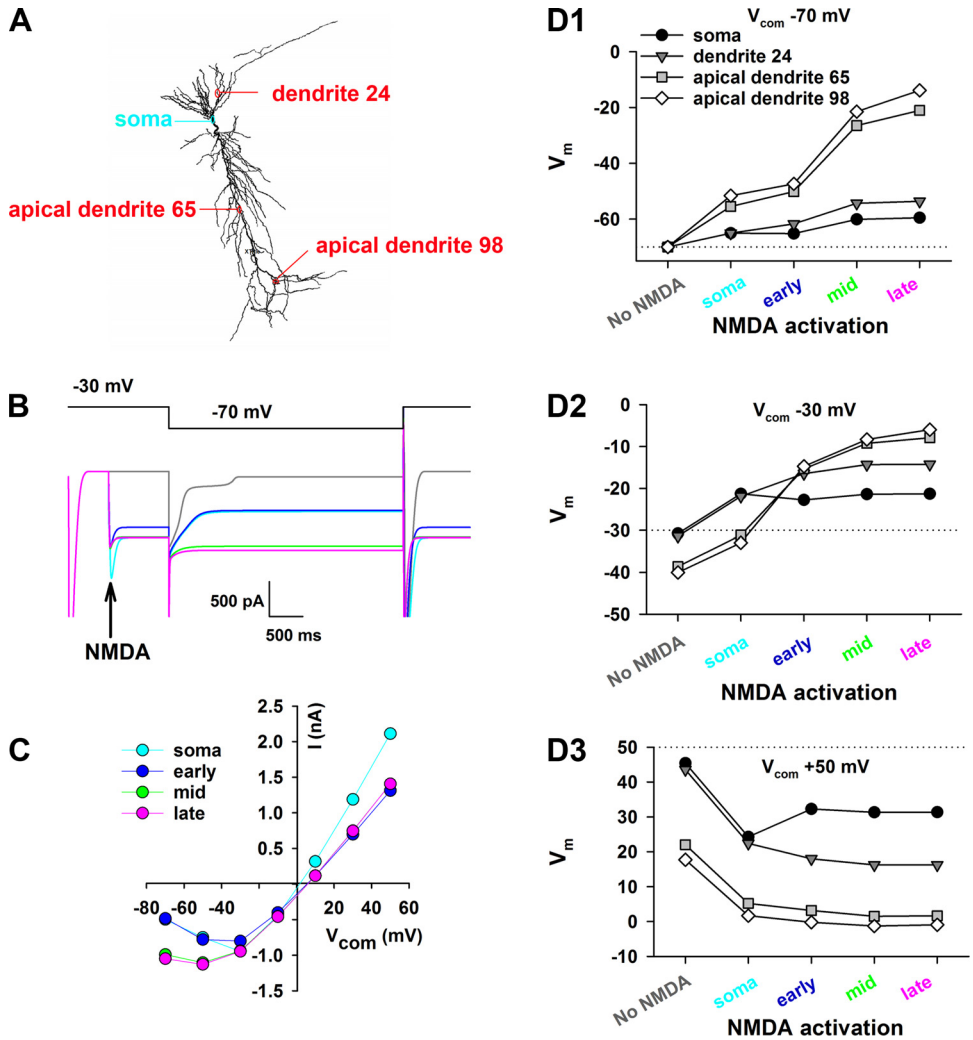

Fig. 5. Simulations demonstrate that linearization can be explained by spatial voltage errors. *A*: model of a previously published CA1 pyramidal neuron (Poirazi et al. 2003a, 2003b) available from the NEURON database. Soma (cyan) and 3 labeled dendrites (red) correspond to plots in *D*. *B*: currents observed in a simulated voltage-clamp experiment in which the NMDAR conductance was applied for the duration of the sweep (arrow indicates NMDA onset) and the command potential was pulsed from −30 mV to −70 mV. Initial inward current represents poorly clamped Ca^{2+} current in the dendrites and soma resulting from initiation of the step to −30 mV. At the onset of the pulse to −70 mV, there is also poorly clamped Ca^{2+} tail current evident in the baseline trace (gray) in the absence of NMDA (NMDA conductance set to 0 in every compartment). Colors of traces represent different levels of total NMDA conductance over the entire model cell to simulate different time points, as indicated in *C*. To show the effect of a well-clamped experiment, we simulated activation of channels only in the somatic compartment. For soma-only simulation (cyan), we used an NMDA conductance density of 12.56 mS/cm^2 in the 5 compartments representing the soma. The conductance value was chosen to approximately match the current generated at −30 mV among simulations below. To simulate early time points (blue), NMDA maximum conductance (g_{max}) density was set to 0.27 mS/cm^2 in the 5 soma compartments and the proximal dendritic segments that are within 50 μm of the soma and 0.145 μS/cm^2 for the remaining dendrites. For the middle time point (green), NMDA conductance in all dendrites was increased to 0.27 mS/cm^2 to match the soma value. For the late (magenta) simulation, NMDA maximum conductance density in the tufts of apical dendrites (>400 μm from soma) was increased to 0.55 mS/cm^2. Capacitive currents have been truncated. *C*: *I-V* relationships for NMDA currents in a simulated voltage-clamp experiment in which the command potential ranged from −70 mV to +50 mV. *D1–D3*: voltage-clamp errors simulated with somatic voltage clamped at −70 mV, −30 mV, and +50 mV, respectively, in the 3 dendrites indicated in *A*, chosen to represent proximal, middle and distal dendrites. *y*-Axis indicates actual membrane potential (V_m) in the indicated compartment. Command potentials are given above each graph and are indicated by the dotted lines. Voltage errors in the soma compartment can be attributed wholly to a simulated 10-MΩ electrode access resistance.

processes deeper in the slice led to significant linearization of the simulated somatic clamp current (Fig. 5, *A–C*). To simulate time-dependent exposure of somatic and dendritic compartments to NMDA, we first set the NMDA conductance density at somatic and proximal dendritic compartments to a moderate value (0.27 mS/cm^2), while at the more distal dendritic compartments the NMDA conductance density was set at a lower value (0.145 μS/cm^2). This simulation mimicked "early" NMDA exposure, when exogenously applied NMDA reached soma and proximal dendrites but had not yet penetrated the slice deeply enough to fully reach the distal processes. Conductance densities were chosen to mimic experimental responses to 10 μM NMDA. The early simulation also resulted in a typical, nonlinear NMDAR *I-V* relationship (Fig. 5, *B* and *C*). We then increased the NMDA conductance density in the distal dendrites to match the density in soma and proximal dendrites (Andrasfalvy and Magee 2001), to mimic "mid" NMDA exposure when NMDA had further reached the distal dendrites. This simulation led to significant linearization of the somatic clamp current (Fig. 5, *B* and *C*). Finally, given that the most distal tufts of dendrites may have up to twice the density of NMDARs of more proximal dendrites and soma (Bittner et

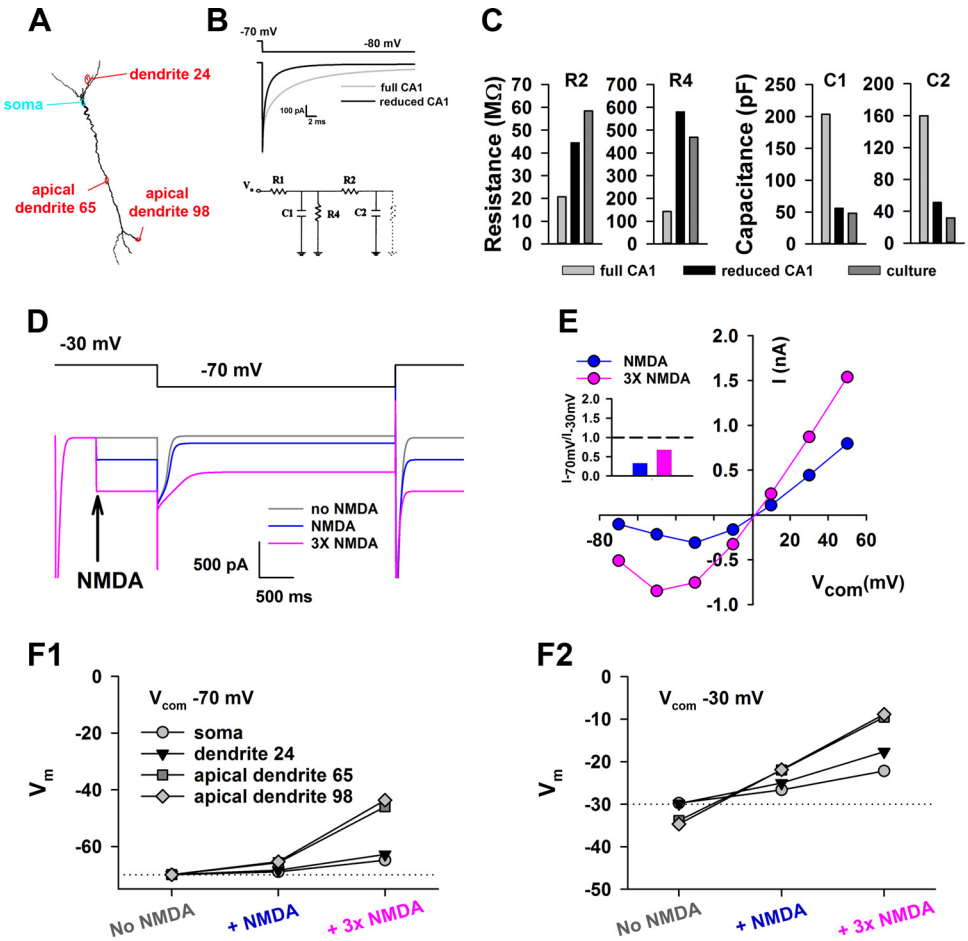

Fig. 6. Simplification of simulation to mimic cultured hippocampal neurons produces a nonlinear NMDA *I-V* relationship. *A*: reduced CA1 model produced by removal of dendritic branches. The "mid" condition from Fig. 5 was retained to simulate NMDA conductance density in the reduced model. *B*: validation of the reduced CA1 model as comparable to cultured neurons. Ten-millivolt hyperpolarizing voltage pulses were simulated (*top* trace). In the full CA1 pyramidal cell model, the resulting capacitive current relaxation (gray trace, *middle*) exhibited a complex, long-lived decay. The capacitive current was speeded with elimination of most dendritic branches (black trace, *middle*). The equivalent circuit (*bottom*) shows a simplified 2-compartment model previously applied to cultured hippocampal neurons (Mennerick et al. 1995). Although simplified relative to the NEURON multicompartment model, the circuit permits solving for the indicated circuit parameters by fitting a biexponential function to the capacitive relaxation (Mennerick et al. 1995). R1 indicates pipette access resistance. C1 (membrane capacitance) and R4 (membrane resistance) represent soma and proximal dendrites. R2 represents the resistance linking the soma and proximal dendrites to distal dendrites, and C2 represents distal dendrite membranes. The dotted resistor in the distal compartment indicates an assumption of a very high resistance of distal dendritic membranes, allowing the equivalent circuit to be solved. See Mennerick et al. (1995) for additional details. *C*: application of the best-fit biexponential function to the simulation (full CA1 and reduced CA1) produced a reasonable match between parameters for the reduced CA1 and the cultured neurons, whose values were taken from a previous report (Mennerick et al. 1995). *D*: simulation as in Fig. 5. Gray trace, current in absence of NMDA; blue trace, current in presence of NMDA at the conductance density used for the "mid" condition in Fig. 5 (0.27 mS/cm^2 throughout); magenta trace, current in presence of NMDA at 3-fold higher NMDA maximum conductance density (0.81 mS/cm^2). *E*: baseline-subtracted NMDA current at indicated maximum conductance density and V_{com}. *Inset*: calculated I_{-70mV}/I_{-30mV} at indicated maximum conductance density. *F1* and *F2*: simulated somatic and dendritic voltage at the indicated V_{com} with or without NMDA application at indicated maximum conductance density. Compared with the full CA1 model, V_m is better maintained in dendrites in the V_{com} range from −70 mV to −30 mV.

al. 2012; Otmakhova et al. 2002), we simulated late, full recruitment of all NMDARs at the most distal dendritic tufts by doubling the NMDA conductance density in only these branches to simulate a later stage of activation (Fig. 5, *B* and *C*). This increase had little additional impact on the *I-V* relationship.

Although the simulation did not produce a linearization as strong as some experimental observations, simulations recapitulated two additional salient aspects of the experimental observations. First, although the reversal potential of simulated NMDAR current shifted slightly with recruitment of small sections of distal dendrites (cyan vs. other traces in Fig. 5*C*), the additional increase in conductance density in dendrites did not further shift the reversal potential. Second, the slope of the *I-V* relationship between −30 mV and +50 mV was not strongly altered despite the increased conductance.

To gain more mechanistic insight into the linearization, we plotted the escape-clamp voltages of representative dendritic segments activated in the simulations (Fig. 5*D*). Increased dendrite NMDA conductance increased voltage error in the distal dendrites relative to the command voltage, such that at the command potential of −70 mV, actual dendritic voltages progressively lose Mg^{2+} block and generate inward current reaching the somatic clamp (Fig. 5, *B* and *D1*). At V_{com} values of −30 mV though +50 mV, distal dendrites stabilize near the reversal potential of 0 mV, thereby contributing little current and explaining the lack of conductance change measured at the soma (Fig. 5, *D2* and *D3*). The increase of conductance in

distal, tufted dendrites in the "late" simulation further depolarized the local V_m of distal dendrites at $V_{com} = -70$ mV (Fig. 5*D1*), but this change was apparently too remote and compartmentalized to strongly influence the overall *I-V* relationship.

Cultured neurons did not exhibit linearization (Fig. 4, *D* and *F*). To test whether the morphology of cultured neurons could explain this, we removed dendrites from the CA1 pyramidal cell model until the passive membrane response of the model approximated that observed for cultured hippocampal neurons (Mennerick et al. 1995). We have previously demonstrated that the capacitive response of cultured neurons to a 10-mV hyperpolarizing voltage pulse (Fig. 6*B*) is adequately described by a biexponential function. The parameters derived from the fit can be used to solve a two-compartment equivalent circuit representation of the cells, with the two compartments related to the soma plus proximal dendrites vs. the distal dendrites, respectively (Fig. 6*B*, *bottom right*; Mennerick et al. 1995). For the full CA1 pyramidal cell model, the estimated capacitance of both the proximal and distal compartments was much larger than the estimates for cultured cells taken from previous work (Fig. 6, *B* and *C*; Mennerick et al. 1995). Also, the resistance of the membrane and resistance linking the two cellular compartments were lower than corresponding values of cultured neurons, likely reflecting the resistive pathways to dendritic branches (Fig. 6*C*, "full CA1"). Although these features are qualitatively expected, we note that using only two compartments to represent a full pyramidal cell is likely quantitatively inadequate. However, after removal of most dendrite branches, the biexponential fit and derived values achieved a reasonable match to cultured cells (Fig. 6*C*, "reduced CA1").

With NMDAR conductance density maintained at the "mid" level from Fig. 5, whole cell NMDA current amplitudes simulated in the reduced CA1 model also reasonably matched those from cultured neurons (Fig. 4*D* vs. Fig. 6, *D* and *E*). We found, as with experimental observations in cultures, that the NMDA *I-V* relationship maintained a strongly nonlinear profile. To examine whether elevation of overall NMDA conductance would alter *I-V* relationship in the simplified morphology, we simulated NMDA currents with threefold higher conductance density in the entire model (Fig. 6, *D* and *E*). Elevation of NMDA conductance density slightly altered the *I-V* curve, estimated by the ratio I_{-70mV}/I_{-30mV} (Fig. 6*E*, *inset*), but the ratio remained well below 1.0. Although increased voltage error in the distal dendrites was observed at the command potential of −70 mV with increased overall NMDA conductance, this alteration only mildly relieved Mg^{2+} block as monitored by somatic clamp (Fig. 6*F1* vs. Fig. 5*D1*). Thus a simplified CA1 morphology with limited dendritic branching, approximating that of cultured neurons, allowed reasonable space clamp to be maintained (Fig. 6, *D* and *F*), even when NMDAR conductance was increased to levels higher than those experimentally observed.

DISCUSSION

We describe the emergence of a time-dependent, NMDA-elicited current at negative V_m in hippocampal CA1 pyramidal neurons from experimental data and simulation. The current depended on ion flow but not on Ca^{2+} influx. Although the current could easily be mistaken for an NMDAR-elicited secondary current or a change in Mg^{2+} sensitivity of NMDARs, key aspects of the behavior can be accounted for by space-clamp error. Sufficiently strong activation of dendrites caused escape from clamp that generated relief from Mg^{2+} block and inward current at negative V_{com}. At positive V_{com}, V_m in NMDA-activated dendrites remained near the NMDAR reversal potential and therefore contributed little current. These properties could easily be mistaken for activation-dependent loss of Mg^{2+} block. Dissociated cells in culture and nucleated patches exhibited little evidence of the same mechanism unless conductance was increased beyond experimentally observed values, befitting better space-clamp conditions. Although poor clamp of dendrites has been previously demonstrated (Bar-Yehuda and Korngreen 2008; Major et al. 1994; Poleg-Polsky and Diamond 2011; Schaefer et al. 2003; Spruston et al. 1993; Williams 2004; Williams and Mitchell 2008), our results show how such errors could specifically contribute to a faulty conclusion that NMDARs are subject to time- and activation-dependent changes in Mg^{2+} sensitivity. The results even pertain to mature DGCs, which are generally considered well-clamped cells with favorable electrotonic properties (Carnevale et al. 1997).

Unlike several previous reports, our results revealed only limited evidence for the induction of secondary currents in response to strong NMDAR activation in juvenile hippocampus. Secondary currents activated by NMDA but mediated by other channels have been reported in dissociated cultures, acutely dissociated neurons, and slices. The secondary conductances have been attributed to gap junction hemichannels, TRP family activation, Ca^{2+}-activated potassium channels, and pannexin channels (Olah et al. 2009; Mrejeru et al. 2011; Thompson et al. 2008; Weilinger et al. 2012, 2016; Zorumski et al. 1989). Secondary current has been suggested to be activated by Ca^{2+} influx, reactive oxygen species, or metabotropic functions of NMDARs (Chen et al. 1997; Mrejeru et al. 2011; Olah et al. 2009; Thompson et al. 2008; Weilinger et al. 2012, 2016). We observed strong bona fide secondary currents in dissociated hippocampal neurons, but CA1 pyramidal neurons in slices exhibited little persisting secondary current (Fig. 2). Although our results differ from those that identified MK-801-insensitive, persisting secondary current (Weilinger et al. 2016), several details of our experimental conditions were not identical. For instance, our study was performed with juvenile mice rather than juvenile rats, and we employed physiological Mg^{2+} in our experiments, while Mg^{2+} was omitted in the experiments of Weilinger et al. Like the previous work, we focused on CA1 pyramidal neurons, and we did not systematically test for persisting currents in dentate granule neurons or interneurons. It remains possible that persisting secondary current contributes to linearization in these cell types.

The time dependence of changes to NMDAR *I-V* curves at 7.5–10 μM NMDA, near NMDA EC_{50} (i.e., 5–10 μM), is perhaps the most difficult feature of our experimental observations to explain. Simulations offer some insight. We assume that NMDA takes longer to reach full concentration at deeply embedded dendrites than the somatic region, which was consistently close to the slice surface to allow visually guided patching. At a V_{com} of −30 mV, progressive increase in dendritic conductance, as the local NMDA concentration increases, adds very little to the somatic clamp current (Fig. 5, *B* and *C*). This is the result of dendrites depolarizing to near reversal potential (Fig. 5*D2*). The decrease of single-channel

current as a result of V_m approaching reversal potential also likely contributes to the signature decrease in membrane noise observed at $V_{com} = -30$ mV (Fig. 1, Fig. 2). However, the added conductance contributes to more variability in dendritic V_m at the V_{com} of -70 mV (Fig. 5*D1*), necessitating more somatic clamp current and leading to linearization. Our results offer a caution that nonsaturating drug concentrations may appear to reach steady state before they actually have.

The apparent loss of Mg^{2+} block in our work could explain some previous observations of secondary current and/or modulation of Mg^{2+} sensitivity under voltage-clamp conditions. Previous observations of reduced Mg^{2+} sensitivity have been performed with cultured neurons (Zhang et al. 1996). Although we did not observe strong space-clamp artifact in our cultures, it is difficult to know whether space-clamp error participates in other culture preparations, where neurons may be more complex morphologically. Some previous investigations of secondary currents have been performed in nominally Mg^{2+}-free bath solutions where the mechanisms explored here would not seem to apply (Chen et al. 1997; Weilinger et al. 2016), but even small amounts of contaminating Mg^{2+} from endogenous sources could lead to effects similar to those described here. The lack of effect of MK-801 inhibition of secondary current in some studies has implied involvement of metabotropic NMDAR function. MK-801 block, like Mg^{2+} block, is voltage sensitive (Huettner and Bean 1988). Although we did not observe evidence for MK-801 insensitivity in our work (Fig. 2, *D* and *F*), under some conditions voltage errors, rather than metabotropic function, could lead to MK-801 insensitivity and erroneous interpretation.

Simulations qualitatively replicated loss of Mg^{2+} block through voltage error, although the experimental loss of block was often quantitatively more severe (Fig. 5*C* vs. Fig. 2*B* and Fig. 4, *A* and *C*). There are several possible explanations for the quantitative mismatch. First, the simulation makes no attempt to model spines and the accompanying spine-neck resistance. Empirical guidance remains insufficient for modeling the electrical resistance of spines (Yuste 2013). Nevertheless, because most NMDARs are likely located on the spine head, neck resistance could dictate how strongly compartmentalized the spine is from the somatic clamp and how well clamped the currents are. Second, we based our distribution of NMDAR conductance on previous work showing that the somatic and dendritic densities of NMDARs are approximately the same. If instead dendritic density (site of most excitatory synapses) is higher than somatic density, this could explain the stronger linearization of experimental currents. Finally, we cannot fully exclude the possibility of some contribution of bona fide change in Mg^{2+} sensitivity.

Several past studies have also cautioned about the poor space clamp of neurons. Typically, this work has focused on the artifacts inherent in clamping phasic excitatory postsynaptic currents or dendritic voltage-gated currents, with attendant electrotonic filtering effects on rapidly rising and decaying currents (Bar-Yehuda and Korngreen 2008; Major et al. 1994; Poleg-Polsky and Diamond 2011; Schaefer et al. 2003; Spruston et al. 1993; Williams 2004; Williams and Mitchell 2008). Our work shows that even steady-state current is badly distorted as a result of poor space clamp over dendrites. Although dendritic conductance loads can be very compartmentalized (Williams 2004), our results (Fig. 5, Fig. 6) demonstrate that the summed impact of a uniform, widespread dendritic conductance change can have a pronounced effect on somatically recorded voltage-clamp currents.

In summary, our work highlights a specific phenomenon accounted for by a space-clamp artifact. It bears resemblance to reduced Mg^{2+} sensitivity of NMDAR function. However, the phenomenon is not evident in simplified experimental preparations and is mimicked in simulations of morphologically complex neurons. Our observations highlight the need to carefully address errors that arise when working with neurons of realistic morphology and complexity, to ensure accurate interpretation.

GRANTS

This work was supported by the Bantly Foundation, by National Institute of Mental Health Grants R01 MH-078823, R01 MH-101874, and R21 MH-104506 (S. Mennerick, C. F. Zorumski), and by a Washington University McDonnell Center for Cellular and Molecular Neurobiology postdoctoral fellowship (M.-Y. Sun).

DISCLOSURES

C. F. Zorumski serves on the Scientific Advisory Board of Sage Therapeutics. Sage Therapeutics was not involved in this work. The other authors declare no conflicts of interest.

AUTHOR CONTRIBUTIONS

M.-Y.S., M.C., L.N.E., and S.J.M. conceived and designed research; M.-Y.S., M.C., and L.N.E. performed experiments; M.-Y.S., L.N.E., and S.J.M. analyzed data; M.-Y.S., L.N.E., and S.J.M. interpreted results of experiments; M.-Y.S. and S.J.M. prepared figures; M.-Y.S. drafted manuscript; M.-Y.S., M.C., L.N.E., C.F.Z., and S.J.M. edited and revised manuscript; M.-Y.S., M.C., L.N.E., C.F.Z., and S.J.M. approved final version of manuscript.

REFERENCES

Anderson CR, Stevens CF. Voltage clamp analysis of acetylcholine produced end-plate current fluctuations at frog neuromuscular junction. *J Physiol* 235: 655–691, 1973. doi:10.1113/jphysiol.1973.sp010410.

Andrasfalvy BK, Magee JC. Distance-dependent increase in AMPA receptor number in the dendrites of adult hippocampal CA1 pyramidal neurons. *J Neurosci* 21: 9151–9159, 2001.

Banke TG, Chaplan SR, Wickenden AD. Dynamic changes in the TRPA1 selectivity filter lead to progressive but reversible pore dilation. *Am J Physiol Cell Physiol* 298: C1457–C1468, 2010. doi:10.1152/ajpcell.00489.2009.

Bar-Yehuda D, Korngreen A. Space-clamp problems when voltage clamping neurons expressing voltage-gated conductances. *J Neurophysiol* 99: 1127–1136, 2008. doi:10.1152/jn.01232.2007.

Bittner KC, Andrasfalvy BK, Magee JC. Ion channel gradients in the apical tuft region of CA1 pyramidal neurons. *PLoS One* 7: e46652, 2012. doi:10.1371/journal.pone.0046652.

Carnevale NT, Tsai KY, Claiborne BJ, Brown TH. Comparative electrotonic analysis of three classes of rat hippocampal neurons. *J Neurophysiol* 78: 703–720, 1997.

Chen L, Huang LY. Protein kinase C reduces Mg^{2+} block of NMDA-receptor channels as a mechanism of modulation. *Nature* 356: 521–523, 1992. doi:10.1038/356521a0.

Chen QX, Perkins KL, Choi DW, Wong RK. Secondary activation of a cation conductance is responsible for NMDA toxicity in acutely isolated hippocampal neurons. *J Neurosci* 17: 4032–4036, 1997.

Chung MK, Güler AD, Caterina MJ. TRPV1 shows dynamic ionic selectivity during agonist stimulation. *Nat Neurosci* 11: 555–564, 2008. doi:10.1038/nn.2102.

Cohen S, Greenberg ME. Communication between the synapse and the nucleus in neuronal development, plasticity, and disease. *Annu Rev Cell Dev Biol* 24: 183–209, 2008. doi:10.1146/annurev.cellbio.24.110707.175235.

Destexhe A, Mainen ZF, Sejnowski TJ. Kinetic models of synaptic transmission. In: *Methods in Neuronal Modeling*, edited by Koch C, Segev I. Cambridge, MA: MIT Press, 1998.

Ferreira LG, Faria RX. TRPing on the pore phenomenon: what do we know about transient receptor potential ion channel-related pore dilation up to now? *J Bioenerg Biomembr* 48: 1–12, 2016. doi:10.1007/s10863-015-9634-8.

Ghasemi M, Schachter SC. The NMDA receptor complex as a therapeutic target in epilepsy: a review. *Epilepsy Behav* 22: 617–640, 2011. doi:10.1016/j.yebeh.2011.07.024.

Hardingham GE, Bading H. Synaptic versus extrasynaptic NMDA receptor signalling: implications for neurodegenerative disorders. *Nat Rev Neurosci* 11: 682–696, 2010. doi:10.1038/nrn2911.

Hestrin S, Nicoll RA, Perkel DJ, Sah P. Analysis of excitatory synaptic action in pyramidal cells using whole-cell recording from rat hippocampal slices. *J Physiol* 422: 203–225, 1990. doi:10.1113/jphysiol.1990.sp017980.

Huettner JE, Bean BP. Block of *N*-methyl-D-aspartate-activated current by the anticonvulsant MK-801: selective binding to open channels. *Proc Natl Acad Sci USA* 85: 1307–1311, 1988. doi:10.1073/pnas.85.4.1307.

Hunt DL, Castillo PE. Synaptic plasticity of NMDA receptors: mechanisms and functional implications. *Curr Opin Neurobiol* 22: 496–508, 2012. doi:10.1016/j.conb.2012.01.007.

Jahr CE, Stevens CF. Voltage dependence of NMDA-activated macroscopic conductances predicted by single-channel kinetics. *J Neurosci* 10: 3178–3182, 1990.

Kilkenny C, Browne WJ, Cuthill IC, Emerson M, Altman DG. Improving bioscience research reporting: the ARRIVE guidelines for reporting animal research. *PLoS Biol* 8: e1000412, 2010. doi:10.1371/journal.pbio.1000412.

Liu X, Tilwalli S, Ye G, Lio PA, Pasternak JF, Trommer BL. Morphologic and electrophysiologic maturation in developing dentate gyrus granule cells. *Brain Res* 856: 202–212, 2000. doi:10.1016/S0006-8993(99)02421-X.

Liu YB, Lio PA, Pasternak JF, Trommer BL. Developmental changes in membrane properties and postsynaptic currents of granule cells in rat dentate gyrus. *J Neurophysiol* 76: 1074–1088, 1996.

Major G, Larkman AU, Jonas P, Sakmann B, Jack JJ. Detailed passive cable models of whole-cell recorded CA3 pyramidal neurons in rat hippocampal slices. *J Neurosci* 14: 4613–4638, 1994.

Mayer ML, Westbrook GL, Guthrie PB. Voltage-dependent block by Mg^{2+} of NMDA responses in spinal cord neurones. *Nature* 309: 261–263, 1984. doi:10.1038/309261a0.

McGrath JC, Drummond GB, McLachlan EM, Kilkenny C, Wainwright CL. Guidelines for reporting experiments involving animals: the ARRIVE guidelines. *Br J Pharmacol* 160: 1573–1576, 2010. doi:10.1111/j.1476-5381.2010.00873.x.

Mennerick S, Que J, Benz A, Zorumski CF. Passive and synaptic properties of hippocampal neurons grown in microcultures and in mass cultures. *J Neurophysiol* 73: 320–332, 1995.

Meyers JR, MacDonald RB, Duggan A, Lenzi D, Standaert DG, Corwin JT, Corey DP. Lighting up the senses: FM1-43 loading of sensory cells through nonselective ion channels. *J Neurosci* 23: 4054–4065, 2003.

Mongiat LA, Espósito MS, Lombardi G, Schinder AF. Reliable activation of immature neurons in the adult hippocampus. *PLoS One* 4: e5320, 2009. doi:10.1371/journal.pone.0005320.

Mrejeru A, Wei A, Ramirez JM. Calcium-activated non-selective cation currents are involved in generation of tonic and bursting activity in dopamine neurons of the substantia nigra pars compacta. *J Physiol* 589: 2497–2514, 2011. doi:10.1113/jphysiol.2011.206631.

Nabavi S, Kessels HW, Alfonso S, Aow J, Fox R, Malinow R. Metabotropic NMDA receptor function is required for NMDA receptor-dependent long-term depression. *Proc Natl Acad Sci USA* 110: 4027–4032, 2013. doi:10.1073/pnas.1219454110.

Nowak L, Bregestovski P, Ascher P, Herbet A, Prochiantz A. Magnesium gates glutamate-activated channels in mouse central neurones. *Nature* 307: 462–465, 1984. doi:10.1038/307462a0.

Olah ME, Jackson MF, Li H, Perez Y, Sun HS, Kiyonaka S, Mori Y, Tymianski M, MacDonald JF. Ca^{2+}-dependent induction of TRPM2 currents in hippocampal neurons. *J Physiol* 587: 965–979, 2009. doi:10.1113/jphysiol.2008.162289.

Otmakhova NA, Otmakhov N, Lisman JE. Pathway-specific properties of AMPA and NMDA-mediated transmission in CA1 hippocampal pyramidal cells. *J Neurosci* 22: 1199–1207, 2002.

Paoletti P, Bellone C, Zhou Q. NMDA receptor subunit diversity: impact on receptor properties, synaptic plasticity and disease. *Nat Rev Neurosci* 14: 383–400, 2013. doi:10.1038/nrn3504.

Perouansky M, Yaari Y. Kinetic properties of NMDA receptor-mediated synaptic currents in rat hippocampal pyramidal cells versus interneurones. *J Physiol* 465: 223–244, 1993. doi:10.1113/jphysiol.1993.sp019674.

Poirazi P, Brannon T, Mel BW. Arithmetic of subthreshold synaptic summation in a model CA1 pyramidal cell. *Neuron* 37: 977–987, 2003a. doi:10.1016/S0896-6273(03)00148-X.

Poirazi P, Brannon T, Mel BW. Pyramidal neuron as two-layer neural network. *Neuron* 37: 989–999, 2003b. doi:10.1016/S0896-6273(03)00149-1.

Poleg-Polsky A, Diamond JS. Imperfect space clamp permits electrotonic interactions between inhibitory and excitatory synaptic conductances, distorting voltage clamp recordings. *PLoS One* 6: e19463, 2011. doi:10.1371/journal.pone.0019463.

Sather W, Dieudonné S, MacDonald JF, Ascher P. Activation and desensitization of *N*-methyl-D-aspartate receptors in nucleated outside-out patches from mouse neurones. *J Physiol* 450: 643–672, 1992. doi:10.1113/jphysiol.1992.sp019148.

Schaefer AT, Helmstaedter M, Sakmann B, Korngreen A. Correction of conductance measurements in non-space-clamped structures: 1. Voltage-gated K^+ channels. *Biophys J* 84: 3508–3528, 2003. doi:10.1016/S0006-3495(03)75086-3.

Shah MM, Haylett DG. K^+ currents generated by NMDA receptor activation in rat hippocampal pyramidal neurons. *J Neurophysiol* 87: 2983–2989, 2002.

Singh P, Doshi S, Spaethling JM, Hockenberry AJ, Patel TP, Geddes-Klein DM, Lynch DR, Meaney DF. *N*-methyl-D-aspartate receptor mechanosensitivity is governed by C terminus of NR2B subunit. *J Biol Chem* 287: 4348–4359, 2012. doi:10.1074/jbc.M111.253740.

Spruston N, Jaffe DB, Williams SH, Johnston D. Voltage- and space-clamp errors associated with the measurement of electrotonically remote synaptic events. *J Neurophysiol* 70: 781–802, 1993.

Thompson RJ, Jackson MF, Olah ME, Rungta RL, Hines DJ, Beazely MA, MacDonald JF, MacVicar BA. Activation of pannexin-1 hemichannels augments aberrant bursting in the hippocampus. *Science* 322: 1555–1559, 2008. doi:10.1126/science.1165209.

Walther H, Lambert JD, Jones RS, Heinemann U, Hamon B. Epileptiform activity in combined slices of the hippocampus, subiculum and entorhinal cortex during perfusion with low magnesium medium. *Neurosci Lett* 69: 156–161, 1986. doi:10.1016/0304-3940(86)90595-1.

Weilinger NL, Lohman AW, Rakai BD, Ma EM, Bialecki J, Maslieieva V, Rilea T, Bandet MV, Ikuta NT, Scott L, Colicos MA, Teskey GC, Winship IR, Thompson RJ. Metabotropic NMDA receptor signaling couples Src family kinases to pannexin-1 during excitotoxicity. *Nat Neurosci* 19: 432–442, 2016. doi:10.1038/nn.4236.

Weilinger NL, Tang PL, Thompson RJ. Anoxia-induced NMDA receptor activation opens pannexin channels via Src family kinases. *J Neurosci* 32: 12579–12588, 2012. doi:10.1523/JNEUROSCI.1267-12.2012.

Williams SR. Spatial compartmentalization and functional impact of conductance in pyramidal neurons. *Nat Neurosci* 7: 961–967, 2004. doi:10.1038/nn1305.

Williams SR, Mitchell SJ. Direct measurement of somatic voltage clamp errors in central neurons. *Nat Neurosci* 11: 790–798, 2008. doi:10.1038/nn.2137.

Wu YN, Johnson SW. Rotenone reduces Mg^{2+}-dependent block of NMDA currents in substantia nigra dopamine neurons. *Neurotoxicology* 30: 320–325, 2009. doi:10.1016/j.neuro.2009.01.002.

Yuste R. Electrical compartmentalization in dendritic spines. *Annu Rev Neurosci* 36: 429–449, 2013. doi:10.1146/annurev-neuro-062111-150455.

Zhang L, Rzigalinski BA, Ellis EF, Satin LS. Reduction of voltage-dependent Mg^{2+} blockade of NMDA current in mechanically injured neurons. *Science* 274: 1921–1923, 1996. doi:10.1126/science.274.5294.1921.

Zorumski CF, Thio LL, Clark GD, Clifford DB. Calcium influx through *N*-methyl-D-aspartate channels activates a potassium current in postnatal rat hippocampal neurons. *Neurosci Lett* 99: 293–299, 1989. doi:10.1016/0304-3940(89)90462-X.